Thermal boundary resistance from transient nanocalorimetry: A multiscale modeling approach

Claudia Caddeo,[1,2,*] Claudio Melis,[3] Andrea Ronchi,[1,2,4] Claudio Giannetti,[1,2] Gabriele Ferrini,[1,2] Riccardo Rurali,[5] Luciano Colombo,[3] and Francesco Banfi[1,2,†]

[1]*Dipartimento di Matematica e Fisica, Università Cattolica del Sacro Cuore, Via dei Musei 41, I-25121 Brescia, Italy*

[2]*Interdisciplinary Laboratories for Advanced Materials Physics (I-LAMP), Università Cattolica del Sacro Cuore, Via dei Musei 41, I-25121 Brescia, Italy*

[3]*Dipartimento di Fisica, Università degli Studi di Cagliari, Cittadella Universitaria, I-09042 Monserrato (CA), Italy*

[4]*Department of Physics and Astronomy, KU Leuven, Celestijnenlaan 200D, 3001 Leuven, Belgium*

[5]*Institut de Ciència de Materials de Barcelona (ICMAB-CSIC), Campus de Bellaterra, 08193 Bellaterra, Barcelona, Spain*

(Received 31 October 2016; revised manuscript received 7 January 2017; published 10 February 2017)

The thermal boundary resistance at the interface between a nanosized Al film and an Al_2O_3 substrate is investigated at an atomistic level. The thermal dynamics occurring in time-resolved thermoreflectance experiments is then modeled via macrophysics equations upon insertion of the materials parameters obtained from atomistic simulations. Electrons and phonons nonequilibrium and spatiotemporal temperatures inhomogeneities are found to persist up to the nanosecond time scale. These results question the validity of the commonly adopted lumped thermal capacitance model in interpreting transient nanocalorimetry experiments. The strategy adopted in the literature to extract the thermal boundary resistance from transient reflectivity traces is revised in the light of the present findings. The results are of relevance beyond the specific system, the physical picture being general and readily extendable to other heterojunctions.

DOI: 10.1103/PhysRevB.95.085306

I. INTRODUCTION

Heat transfer at the meso/nanoscale represents an outstanding challenge, among the most relevant under an applicative standpoint [1–4]. In this context thermal boundary resistance (TBR), the parameter ruling heat transfer at the interface between two materials [5], plays a key role. Accessing the TBR between nanosized metals and insulating substrates remains an open issue and the prerequisite to enhance heat dissipation in next-generation micro- and nanodevices. Indeed low thermal dissipation across heterojunctions is among the main impediments towards further circuits downscaling [6,7].

Much effort has been devoted to access the TBR at metal-insulator interfaces both theoretically and experimentally [1,3,8]. Unfortunately theoretical predictions deviate from TBR values extracted from time-resolved thermoreflectance (TR-TR) measurements [9,10], the go-to technique to inspect TBR at these junctions [11–16]. The present work, based on multiscale modeling, reconciles the discrepancy for the paradigmatic case of the Al-sapphire heterojunction.

The basic idea to extract the TBR from a metal-dielectric interface via a TR-TR experiment is as follows. A short laser pump pulse delivers energy to the metallic film, triggering an impulsive temperature dynamics. The temperature dynamics (a) is ruled by the materials thermal parameters, among which the TBR, and (b) affects the temperature-dependent optical constants of the sample resulting in a transient reflectivity variation. The latter is investigated by means of time-delayed laser probe pulses, the time-delay being with respect to the excitation instant. The information on the TBR is ultimately encoded in the sample's transient reflectivity changes. In order to retrieve the TBR a model linking the TBR to the thermal dynamics is thus required.

Typically the metal film is modeled as a lumped thermal capacitance [17] exchanging heat with the underlying dielectric substrate through a TBR. This implies a unique time-varying film temperature (electrons and phonons anchored at the same temperature), constant throughout the film thickness. The reflectivity variation is then linked to the film's spatially homogenous temperature profile.

In the present work we challenge the validity of this model for values of the TBR that might be expected at solid-solid interfaces and argue that its application in the fitting procedure of the time-resolved reflectivity traces leads to an overestimation of the true TBR. We adopt multiscale modeling to rationalize the thermal dynamics occurring in TR-TR measurements. On this basis a procedure to extract the TBR from transients experiments is proposed.

The present approach is based on atomistic modeling of the TBR and the subsequent description of the impulsive thermodynamics beyond the lumped thermal capacitance approach. The onset of spatiotemporal temperatures gradients in the metal film during all-optical time-resolved nanocalorimetry experiments is shown. TR-TR experiments probe a temperature dynamics—taking place in proximity of the metal film surface—other than the one controlling the TBR—occurring at the film interface. Based on this evidence a strategy is put forward to extract the TBR from TR-TR traces. The emerging physical picture and the TBR retrieval protocol are rather general and may find application in a variety of interfaced systems in addition to the present one.

The work is organized following a bottom-up progression both in dimensions and time scales. In Sec. II the suitability of the Al-Al_2O_3 heterojunction is briefly addressed. In Sec. III the material thermal parameters—TBR and lattice thermal conductivities—are calculated at an atomistic level by nonequilibrium molecular dynamics (NEMD). Theoretical

*caddeo@iom.cnr.it
†francesco.banfi@unicatt.it

assessment of the TBR is of paramount importance since its value influences the impulsive thermal dynamics occurring in TR-TR experiments. Attention is therefore devoted to validate the results by inspecting the temperature dependence of the TBR and verifying its truly interface character. We pinpoint that if, instead of the theoretically calculated TBR values, we were to rely on the experimental values of the TBR as retrieved from previous TR-TR measurements (that is obtained by fitting the experimental data with a lamped thermal capacitance model) we would run the risk of forcing the temperature distribution to be spatially homogeneous, conformally to the ansatz behind the fitting model. This concept is discussed in Sec. IV, that addresses the thermal dynamics occurring in TR-TR experiment via continuous macrophysics equations (Sec. IV A) and its link to both the transient thermoreflectivity traces and the TBR retrieval process (Sec. IV B). The modeling, based on finite element methods (FEM), involves the interplay of Maxwell equations, the two-temperature model (TTM), and Fourier law for heat transport with insertion of the material thermal parameters calculated from NEMD. The implication of the thermal dynamics on TR-TR experiments, and on the TBR therein accessed, are theoretically discussed. An effective TBR retrieval protocol is proposed, readily extendable to other interfaces. Finally (Sec. IV C), the present findings are discussed in the light of recent literature results in the frame of steady-state heat transfer.

II. WHY THE Al-Al_2O_3 HETEROJUNCTION

The Al-Al_2O_3 interface represents an ideal model system to address the issue at hand. Sapphire is optically transparent whereas Al absorbs energy over a wide spectral range—UV to the IR—allowing for selective heating of the metal film only upon laser pulse absorption. Sapphire has no porosity nor grain boundaries, thus allowing for a well defined interface, a key feature needed to minimize the possible influence of roughness-driven phonon scattering pathways on the TBR. For this materials combination, the effect of direct electron-phonon coupling across the interface on the TBR may be disregarded [18]. Experimental TBR data, as retrieved from TR-TR measurements, are available in the literature [11]. These aspects allow focusing on the relevant physics avoiding unnecessary complications. Nevertheless, the emerging physical picture is rather general and may apply to heterojunctions other than the present one.

Assessment of the thermal parameters in this system has an immediate technological fallout. The TBR between an Al thin film and the supporting sapphire is of relevance in a variety of applications ranging from broad-band optical mirrors [19] to high frequency optoacoustic transducers [20] and protective coatings technology [21].

III. MATERIALS THERMAL PARAMETERS FROM ATOMISTIC MODELING

In this section the materials thermal parameters—TBR and lattice thermal conductivities—are calculated at an atomistic level on a system of realistic size. The outcome will then serve as the input for modeling the impulsive thermodynamics taking place in TR-TR experiments as addressed in Sec. IV.

A. Nonequilibrium molecular dynamics

NEMD [22] has been used to calculate the lattice thermal conductivity of the pure Al thin film, of the pure Al_2O_3 substrate, and to determine the TBR, R_{ph}. The subscript recalls that the TBR in this system is solely determined by phonons, as will be addressed further on. In brief, NEMD consists in coupling the opposite ends of the sample to two thermostats at different temperature, T_{hot} and T_{cold}, in order to generate a stationary thermal conduction regime. The heat flux $\mathbf{J_i}(\mathbf{J_r})$ injected into (removed from) the sample is calculated as the numerical time derivative of the energy injected into (removed from) the sample per unit area [23]. Heat transport is here one dimensional and takes place along the z axis. From now on the heat flux will therefore be casted in scalar form. When steady state is reached, $|\mathbf{J_i}| = |\mathbf{J_r}| = |J|$, J being the steady-state heat flux. The steady-state temperature spatial profile $T(z)$ is calculated starting from the atomic kinetic energy via the equipartition theorem. The steady-state temperature gradient dT/dx is hence retrieved. With these two ingredients at hand the thermal conductivity, κ, is finally obtained by applying the scalar version of Fourier law

$$J = -\kappa \frac{dT}{dz}. \tag{1}$$

The same method can be applied to interfaced systems to obtain the TBR. When a stationary state is reached, a temperature drop $\Delta T = T_{ih} - T_{ic}$ at the interface can be observed, due to the presence of a TBR, T_{ih} and T_{ic} being the temperatures on the hot and cold side of the interface, respectively. R_{ph} is calculated according to

$$R_{\mathrm{ph}} = \frac{\Delta T}{|J|}. \tag{2}$$

1. Sample preparation

Al_2O_3 can be found in different crystalline phases, among which α-Al_2O_3 (corundum) is the most stable one at ambient conditions. We simulated this phase with the heat flux flowing along the (0001) direction.

In many crystalline systems [24,25], the lattice thermal conductivity, κ_{ph}, depends on the sample length, L_z, along the heat flux direction. This is because, if L_z is shorter than the maximum phonon mean free path λ_{max}, phonons with mean free path in the range $L_z < \lambda < \lambda_{\mathrm{max}}$ will not contribute to κ_{ph}. Since the experimental setup involves bulk Al_2O_3 and thin Al films, we need to estimate the minimum Al_2O_3 thickness which is able to appropriately mimic the thermal behavior of bulk sapphire. We have thus generated Al_2O_3 samples of different length, L_z, and we have calculated their lattice thermal conductivity. It has been shown [26] that R_{ph} is substantially unaffected by the dimensions of the samples in the directions perpendicular to the heat flux. Furthermore, in order to assess if this condition is fulfilled also by our system, we performed a convergence test on samples with a doubled lateral size and we did not observe sizable variations in the value of R_{ph}. For computational convenience we have thus chosen to fix the lateral size of our samples to $L_x = 2.47$ nm and $L_y = 2.86$ nm. L_z was varied between 20 and 200 nm.

In general, the overall thermal conductivity κ is given by the sum of lattice and electronic contributions, $\kappa = \kappa_{\mathrm{ph}} + \kappa_e$. For

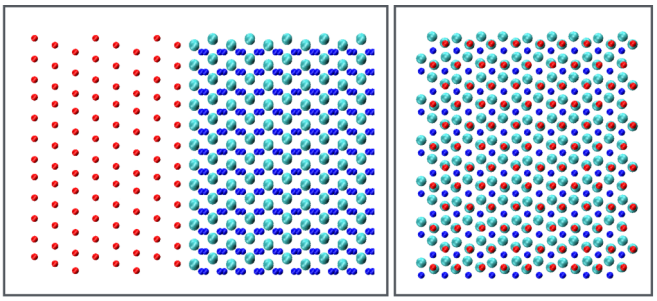

FIG. 1. Model for the Al/Al_2O_3 interface. Cyan represents oxygen, blue corresponds to Al atoms in sapphire, and red to Al in the metal slab. Left (right) panel shows the side (top) view.

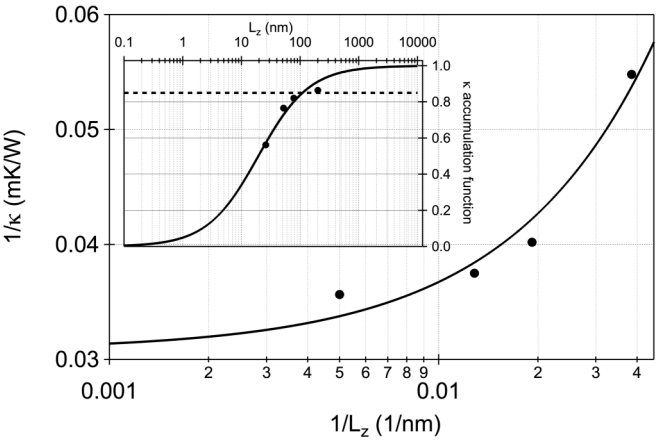

FIG. 2. Black dots: reciprocal of lattice thermal conductivity of pure Al_2O_3 vs reciprocal Al_2O_3 length. Black continuous line: fitting function $1/\kappa(L_z) = (1/\kappa^{\infty})[1 + (\lambda/L_z)]$ from which κ^{∞} is extrapolated. (Inset) Black dots: κ accumulation function, $\kappa(L_z)/\kappa^{\infty}$, for pure Al_2O_3 vs Al_2O_3 length (top axis). Black continuous line is the function $\kappa(L_z)/\kappa^{\infty} = [L_z/(\lambda + L_z)]$. Gray dashed horizontal line represents 85% of the accumulation function. In both graphs the abscissa are in log scale.

thermal insulators, such as Al_2O_3, the electronic contribution is however negligible, and thus $\kappa \approx \kappa_{ph}$. From now on, we will use κ when referring to the conductivity of Al_2O_3, while we will distinguish κ_{ph} and κ_e when addressing Al.

As far as concerns the Al/Al_2O_3 interface, among the possible models proposed [27–32] we choose the one suggested by Mei *et al.* [32] that was found to be the most stable for the Streitz-Mintmire potential. In detail, the orientation relationship between Al and sapphire is $[\bar{1}10](111)_{Al}||[10\bar{1}0](0001)_{Al_2O_3}$, the sapphire is O-terminated, and the Al atoms are located on top of the O atoms of the sapphire surface. Al/Al_2O_3 interfaces were constructed by coherent lattice approximation following Ref. [32] (see Fig. 1).

B. Lattice thermal conductivity of Al_2O_3 and Al

The room temperature thermal conductivity of pure Al_2O_3 is calculated for 20 nm $\leqslant L_z \leqslant$ 200 nm. In order to estimate the value of κ for $L_z = \infty$ we use the usual $1/\kappa$ vs $1/L_z$ linear extrapolation procedure [24], obtaining $\kappa^{\infty} = 32.5$ W m^{-1}K^{-1}, in excellent agreement with the experimental value [33] of 35 W m^{-1}K^{-1}. The results are reported in Fig. 2. The inset of the same figure shows the corresponding accumulation function, defined as the ratio $\kappa(L_z)/\kappa^{\infty}$ between the lattice thermal conductivity calculated for a simulation cell with length L_z and the corresponding extrapolated value for $L_z = \infty$. The quantity $\kappa(L_z)/\kappa^{\infty}$ gives the contribution to lattice thermal conductivity provided by phonons with mean free path λ up to L_z. From the behavior of the accumulation function it is apparent that phonons with $\lambda \leqslant 200$ nm contribute to 85% of the thermal conductivity (see dashed horizontal line). Furthermore, for greater sample lengths the accumulation function flattens out. A sample length of 200 nm is a good break-even value beyond which the thermal conductivity may be thought as having reached its asymptotic value. Longer samples would lead to marginal improvements in the thermal conductivity value while requiring prohibitive calculation times. Furthermore, it has been estimated that the maximum phonon mean free path in sapphire is of the order of 100–150 nm at room temperature [13]. Therefore, our 200 nm sample is long enough to accommodate a diffusive transport regime. Our samples will thus consist of an α-Al_2O_3 block of size $2.47 \times 2.86 \times 200$ nm^3 in the x, y, and z directions, respectively, interfaced to a fcc Al block with the same x and y sizes and variable length along the heat flux direction z. From now on we will address the sapphire length L_z simply as L, the lateral dimensions L_x and L_y remaining unchanged throughout the paper. We remark that the good agreement between the estimated bulk thermal conductivity of Al_2O_3 and the available experimental data is observed despite the fact that the present MD simulations miss any quantum features, which are expected to occur below the Debye temperature. This feature is common to other investigations in both bulklike and 2D materials [34,35] and it has been tentatively attributed to the compensation between two opposite errors provided by classical simulations, namely: shorter phonon lifetimes and larger single-phonon contributions to heat capacity than real quantum ones.

Concerning the room temperature lattice thermal conductivity of pure Al, k_{ph}, we find a very weak dependence on L_{Al} in the range 26 to 100 nm, with a value of $k_{ph} \approx 7$ W m^{-1}K^{-1}. This is in agreement with recent *ab initio* calculations on phonon and electron transport properties of Al, showing that phonons with mean free path smaller than 20 nm contribute to 90% of the lattice thermal conductivity [36]. We also notice that our NEMD value is in very good agreement with the *ab initio* one, the latter being $\approx$6 W m^{-1}K^{-1} [37].

C. Thermal boundary resistance

The first studied system corresponds to an interface between a 200 nm thick Al_2O_3 sample and a 60 nm thick Al film and contains $\approx 2 \times 10^5$ atoms. The system has been first relaxed with a conjugated gradient minimization, followed by a low temperature (1 K) short dynamics (5 ps). Atomic partial charges of the whole system have been calculated during the conjugated gradient minimization run.

After relaxation, the system has been coupled to two thermostats of length equal to 12 nm and 40 nm for the Al and Al_2O_3 sides, respectively (corresponding to 20% of

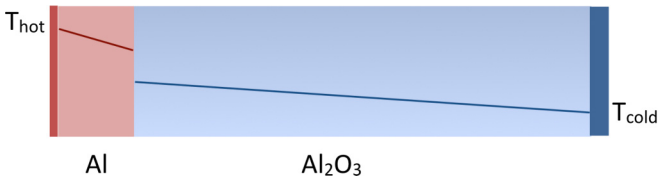

FIG. 3. Schematic representation of the NEMD setup (not to scale). Aluminium is heated by the thermostat set at $T = T_{hot}$, while sapphire is kept at lower temperature by the thermostat set at $T = T_{cold}$.

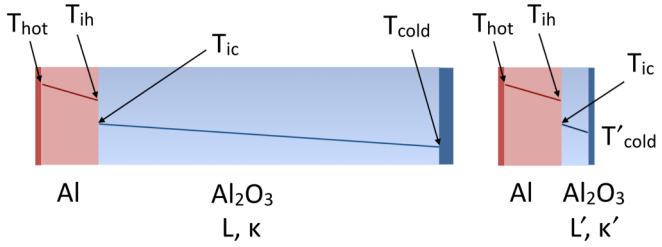

FIG. 4. Illustration of the sapphire thickness reduction strategy.

the metal and insulator region extents). This situation is schematically illustrated in Fig. 3. We choose $T_{hot} = 350$ K and $T_{cold} = 250$ K. For this system steady state is reached after 4.5 ns and the simulation runs for further 1 ns, during which J and ΔT are calculated. The obtained value for $R_{ph} = 1.35$ m^{2}K/GW.

1. Strategy to reduce the computational workload

Since the simulations described in the previous section have been in fact very computer intensive, in view of further calculations we developed a strategy aimed at reducing the overall system size, still predicting correct TBR values. The idea is to perform calculations on a shorter model system while preserving the same R_{ph}. This is achieved by considering that R_{ph} only depends on J and ΔT at the interface, which, in turn, depends on T_{ih} and T_{ic}. We proceed by keeping the Al side unaltered while varying the sapphire substrate extension, L, and the cold thermostat temperature, T_{cold}, under the constraints of constant values of T_{ic} and J.

Upon reducing the thickness of the sapphire slab from L to L', the thermal conductivity on the sapphire side diminishes from κ to κ' due to the size effect described in Sec. III A 1. Requiring T_{ic} to remain constant, T_{cold} is left as the only quantity that may be varied in order to control the heat flux addressed in Fourier law. The thermostat temperature in the reduced slab, T'_{cold}, is then chosen enforcing the heat flux to be independent of slabs length:

$$-\kappa' \frac{(T_{ic} - T'_{cold})}{L'} = -\kappa \frac{(T_{ic} - T_{cold})}{L} \tag{3}$$

yielding

$$T'_{cold} = T_{ic} + \frac{\kappa}{\kappa'} \frac{L'}{L} (T_{cold} - T_{ic}) \tag{4}$$

with κ', L', T_{ic}, and T_{cold} being fixed.

The procedure is illustrated in Fig. 4, where the two equivalent systems are represented.

We have thus reduced the sapphire thickness of our sample from $L = 200$ nm to only $L' = 26$ nm. For the former case calculations yield $\kappa = 28.05$ W m^{-1}K^{-1}, whereas for the latter the value $\kappa' = 18.25$ W m^{-1}K^{-1} is found. The value T_{ic} is fixed at 284 K, as obtained for the sample characterized by L, κ, and T_{cold}. These values, inserted in Eq. (4), yield $T'_{cold} = 276.2$ K. The calculated value for R_{ph} with these new parameters is 1.33 m^{2}K/GW, that is, within the numerical error, equal to the value calculated adopting the thicker substrate. This strategy allowed us to reduce the computational time to one-fifth with respect to the previous case. All the following calculations are performed with the equivalent sapphire length $L' = 26$ nm. We remark that previous works have in fact shown that the value of R_{ph} provided by NEMD simulations is strongly dependent upon system size [8,38]. However, in those works the size effect was evaluated by keeping the heat flux constant while changing the system length, and thus the interface temperatures (due to the size dependence of κ). Here the target is different and, therefore, we follow a different approach, namely we set either the heat flux, the interface temperature, and ΔT to the same value in both cases, i.e., for both the long and the short sample. The resulting R_{ph}, which only depends on J and ΔT, is thus equal in the two samples.

The present length-reduction strategy may be adopted on any interface system providing a substantial gain in computational time. We remark that it is a valid methodology to study interface properties, but it could not be applied to reduce the calculations for the determination of the bulk thermal conductivity.

2. Dependence on film thickness and interface temperature

In order to evaluate the dependence of the TBR on metallic films thicknesses commonly encountered in TR-TR experiments, R_{ph} is here calculated for an Al thicknesses L_{Al} in the range 20–100 nm, keeping the hot and cold thermostats at $T_{hot} = 350$ K and $T'_{cold} = 276.2$ K, respectively, and adopting a 26 nm thick sapphire slab ($L' = 26$ nm). The results are reported in Fig. 5. The values of R_{ph} are constant irrespective of the Al thickness; see left axis in Fig. 5. By augmenting L_{Al} one potentially reduces the interface temperature T_i, where

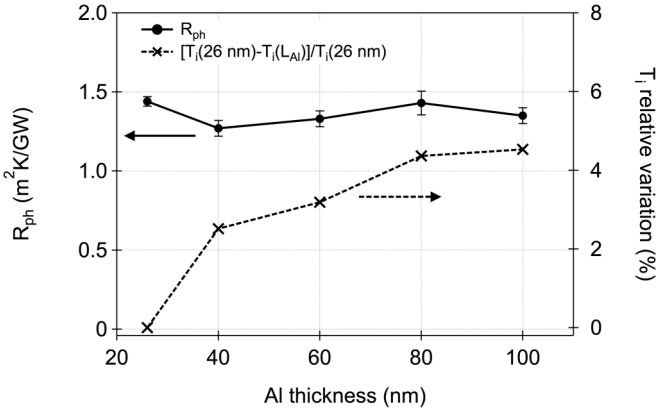

FIG. 5. Thermal boundary resistance (left axis) and relative interface temperature variation (right axis) vs Al thickness.

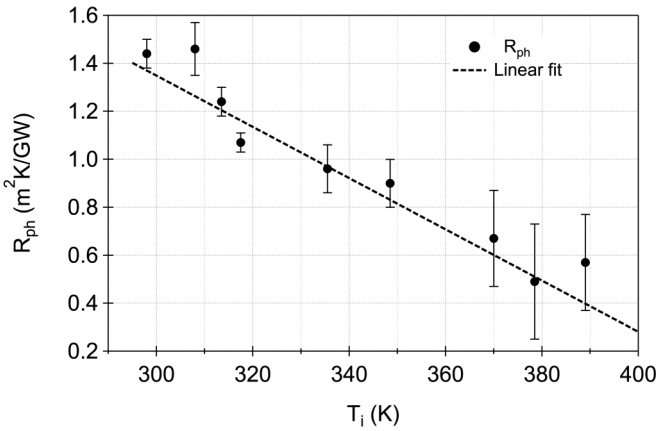

FIG. 6. Thermal boundary resistance $R_{\rm ph}$ vs interface temperature T_i.

$T_i = (T_{ih} + T_{ic})/2$. The question then arises as to whether $R_{\rm ph}$ remains constant because of a combined effect of increasing $L_{\rm Al}$ and decreasing T_i. The percentage variation of T_i with respect to the value calculated for a 26 nm thick Al film, $[T_i(26\ \text{nm})\text{-}T_i(L_{\rm Al})]/T_i(26\ \text{nm})$, is reported against $L_{\rm Al}$ on the right axis of Fig. 5, the maximum interface temperature variation amounting to 4% only. The interface temperature remains basically constant while the film thickness is varied by a factor of 4, thus ruling out the scenario brought about by the aforementioned question. This proves that $R_{\rm ph}$ is a genuine interface property not influenced by the sample length. Similar results have been found for other systems, e.g., for strongly coupled interfaces between crystalline silicon and amorphous silica [39].

We now inspect the temperature dependence of $R_{\rm ph}$ in the range 300 K $< T_i <$ 400 K, the latter being the interface temperature range reached with typical lasers parameters used in TR nanocalorimetric experiments performed at room temperature [15,40–42]. The interface temperature T_i is varied by changing the thermal bath temperature $T_{\rm hot}$ on the film side while keeping $T'_{\rm cold} = 276.2$ K. For computational convenience, we investigate the thinner film sample, $L_{\rm Al} = 26$ nm. Figure 6 reports the calculated values of $R_{\rm ph}$ versus T_i together with the best linear fit (the linear coefficient is equal to -0.011 m^2/GW). The linear decrease of $R_{\rm ph}$ with increasing T_i is observed also in experiments, and with a similar slope [43]. The decrease of $R_{\rm ph}$ with increasing T_i has been observed experimentally also for other kinds of interfaces [15,44], both theoretically [24,39] and experimentally [9,45,46], and it has been attributed to the increment in phonon population (if below the Debye temperature) and also to the increase of the anharmonicity of the atomic interactions with temperature [39,43]. The correct scaling of TBR with temperature is a strong consistency check further confirming the validity of the adopted computational approach.

A comment is due here regarding the eventual role on the TBR of direct coupling of metal electrons and insulator phonons at the interface. Our model solely accounts for the contribution of lattice vibrations to the thermal transfer across the interface. The underlying idea is that electrons cannot flow into the insulator side and therefore should not appreciably contribute. The question then arises as whether, in the absence of electrons flow into the substrate, metal electrons may efficiently couple to the substrate lattice vibrations directly at the interface. This point and its implications on the TBR are a debated issue [18,47]. Let us assume the latter scenario. The metal electrons *directly* couple to nearby phonons at the insulator side, contributing a heat flux $R_e^{-1}(T_{ih,e} - T_{ic})$, where $T_{ih,e}$ is the electron temperature at the metal side of the interface and R_e is the electronic thermal boundary resistance. This energy flux is in *parallel* with that one carried by phonons, which is addressed in NEMD simulations. The electronic thermal boundary conductance, R_e^{-1}, is to be added to the lattice one, $R_{\rm ph}^{-1}$. In the case of the Al/Al_2O_3 interface, and within the frame of the Sergeev model [48], one obtains $R_e^{-1} = 0.64$ GW m^{-2}K^{-1} yielding a value of TBR $= R_{\rm ph}R_e/(R_{\rm ph} + R_e) \approx 0.75 \times R_{\rm ph}$. The Sergeev model tends to overestimate the electron thermal conductance [18]; for this reason an even smaller correction to the TBR is expected. Experimental evidences, obtained engineering the interface quality, also suggest the phonon channel as the dominant heat transfer mechanism across the interface [11]. For these reasons in the following we will stick to the original ansatz, forgoing the role of electron-phonon coupling across the interface and identifying the TBR with $R_{\rm ph}$.

IV. TRANSIENT NANOCALORIMETRY

Knowledge of the material thermal parameters, as obtained from atomistic simulations, now allows us to theoretically address the impulsive thermal dynamics occurring in time-resolved all-optical calorimetry and the associated TBR retrieval process from transient thermoreflectivity traces.

In a typical TR-TR experiment a thin metallic film is placed in thermal contact with a substrate serving as a thermal bath. An ultrafast laser pump beam delivers an energy density ΔU_V to the film triggering an impulsive thermal dynamics (*excitation*). The carriers thermal dynamics affects the temperature dependent dielectric constant, ultimately resulting in a transient sample reflectivity $\Re(t)$. The sample's temperature relaxation to the substrate is accessed measuring the transient reflectivity variation, $\Delta\Re(t)$, via a time-delayed laser probe beam (*detection*). The time delay, t, is taken with respect to the instant of the pump beam arrival and $\Delta\Re(t) = \Re(t) - \Re_0$, where $\Re_0$ is the sample reflectivity in the absence of the excitation process [or equivalently $\Re_0 = \Re(\infty)$ the reflectivity of the sample once relaxed back to equilibrium]. Fitting $\Delta\Re(t)$, with the TBR as the fitting parameter, allows for retrieving the TBR itself. It is therefore essential to link (a) $R_{\rm ph}$ to the carriers thermal relaxation triggered in the *excitation* process (b) the carriers thermal relaxation to the optical reflectivity variation $\Delta\Re(t)$, as acquired in the *detection* process.

A. Excitation process: Impulsive thermodynamics

1. Problem formulation

The physics is addressed considering an Al thin film, 26 nm thick, deposited on a sapphire substrate, 100 μm thick. The overall sample is assumed of cylindrical shape, the diameter being in the mm range. The cylindrical sample cross section is schematically reported in the inset of Fig. 7.

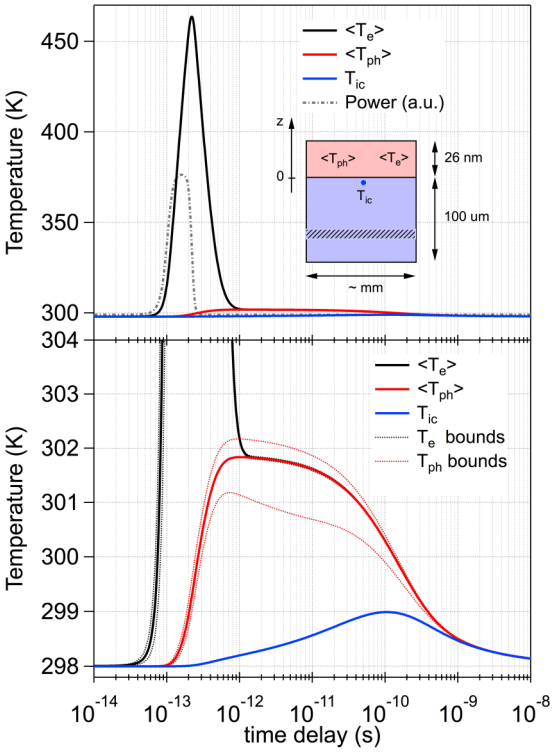

FIG. 7. (Top panel) Average electron (black) and phonon (red) temperatures in the Al film and substrate interface temperature (blue) as a function of the time delay from the leading edge of the laser pulse (gray dash-dotted line) triggering the thermal dynamics. The averages are calculated across the film thickness. Laser pulse power time profile is reported in arbitrary units. (Inset) Schematic of the simulation cell. (Bottom panel) Zoom of the thermal dynamics reported in the top panel up to a temperature range of 304 K. The phonon and electron temperatures across the film thickness are bounded by the dotted red and dotted black curves, respectively. The upper dotted curves are calculated at the Al film free standing surface, the lower dotted curves at the Al interface with Al_2O_3. The dotted black curves coincide with the black curve for delay longer than 100 femtoseconds, the electron temperatures being spatially constant for longer delay times. The delay time is reported in log scale.

Insulating boundary conditions are applied on the top and lateral boundaries whereas the sapphire bottom boundary ($z = -100\ \mu$m) is kept at a constant temperature (as would be the case for a substrate adhering to a temperature controller).

Let us consider a scenario where the sample is excited by a single laser pulse: 5 nJ per pulse, 120 fs time duration at full width half maximum (FWHM), 780 nm central wavelength, 55 μm spatial extension at FWHM. The laser probe beam diameter in real experiments is much smaller than the pump one so as to ensure investigation of an homogeneously excited area. The thermal dynamics will be here discussed in the probed area. For this reason, and for the sake of simplicity, in the present discussion the equations will be casted as if the problem was one-dimensional (1D). In the actual numerics the equations were solved in vectorial form to properly account for boundary conditions on the lateral sample frontiers and the laser spatial Gaussian beam profile. It was then checked that, within the probed area, the problem solutions were in fact 1D.

Within the frame of the two temperature model (TTM) [49] and Fourier law, energy balance within the volume of the metal film reads

$$C_{el}(T_{el})\frac{\partial T_{el}}{\partial t} = P_p(z,t) - G(T_{el} - T_{\rm ph}) + \kappa_e \frac{\partial^2 T_{el}}{\partial z^2}, \quad (5)$$

$$C_{\rm ph}\frac{\partial T_{\rm ph}}{\partial t} = G(T_{el} - T_{\rm ph}) + \kappa_{\rm ph}\frac{\partial^2 T_{\rm ph}}{\partial z^2}, \quad (6)$$

where $C_{\rm ph} = 2.48 \times 10^6$ J/m^{3}K [50], and $C_{el} = \gamma_e T_e$ are the film phononic and electronic specific heat per unit volume, respectively, $\gamma_e = 95$ J m^{-3}K^{-2} is the Sommerfeld parameter for Al calculated starting from the data provided in Ref. [51] and in good agreement with the value reported in Ref. [52], $G = 2.45 \times 10^{17}$ W/m^{3}K is the electron-phonon coupling constant [53], $\kappa_e = 230$ W m^{-1}K^{-1} is the Al electronic thermal conductivity [54], $\kappa_{\rm ph} = 7.12$ W m^{-1}K^{-1} as calculated in Sec. III, and P_p is the profile of the pulsed power per unit volume absorbed by the film electrons [55]. P_p has been calculated accounting for thin film effects via Fresnel relations for a multilayer system assuming $\tilde{n}_{\rm Al} = 2.58 + 8.4i$ and $\tilde{n}_{Al_2O_3} = 1.76$ for the Al and Al_2O_3 indices of refraction at a wavelength of 780 nm; see Refs. [56,57] (we refer to Appendix B for further details). The film is not energetically isolated; phonons can in fact transfer energy across the interface to the sapphire substrate whereas no electrons can flow into the insulator. The heat flux at the Al-Al_2O_3 interface is ruled by $R_{\rm ph}$, as obtained in Sec. III, through the following boundary condition:

$$\begin{aligned} -\kappa_{\rm ph}\frac{\partial T_{\rm ph}}{\partial z}\bigg|_{z=0+} + [T_{\rm ph}(z=0+) - T(z=0-)]/R_{\rm ph} = 0, \\ -\kappa\frac{\partial T}{\partial z}\bigg|_{z=0-} + [T_{\rm ph}(z=0+) - T(z=0-)]/R_{\rm ph} = 0, \end{aligned} \quad (7)$$

with T indicating the substrate temperature, whereas a zero flux boundary condition applies for electrons:

$$-\kappa_e\frac{\partial T_e}{\partial z}\bigg|_{z=0+} = 0. \quad (8)$$

Given the coordinate system specified in the inset of Fig. 7, $z = 0+$ and $z = 0-$ indicate the metal and substrate side of the interface, respectively. We set $R_{\rm ph} = 1.44$ m^{2}K/GW (interesting enough any other value within the fluctuation range reported in Fig. 5 yields the same results [58]), and $\kappa = \kappa^\infty = 32.5$ W m^{-1}K^{-1} as calculated in Sec. III. We remark that $T_{\rm ph}(z=0+)$ and $T(z=0-)$ coincide with the previously defined T_{ih} and T_{ic}, respectively. The thermal dynamics in the sapphire volume is described by the heat equation:

$$C\frac{\partial T}{\partial t} - \kappa\frac{\partial^2 T}{\partial z^2} = 0, \quad (9)$$

where $C = 3.09 \times 10^6$ J/m^{3}K is the sapphire specific heat per unit volume [59]. As for the initial conditions we have assumed a spatially constant temperature $T_0 = 298$ K throughout the sample [60]. The nonlinear system of equations has been solved via the finite element method covering a time scale

spanning five orders of magnitude. For ease of consultation, the materials parameters employed in the FEM simulation are summarized in Appendix C.

2. Results and discussion

A general overview of the relevant thermal dynamics, triggered by the pump laser pulse (black dash-dotted line), may be appreciated inspecting the top panel of Fig. 7. The average electrons, $\langle T_e \rangle$ (black line), and phonons, $\langle T_{\rm ph} \rangle$ (red line), temperatures as calculated across the Al film thickness are therein reported together with the temperature T_{ic} at the Al_2O_3 side of the interface (blue line). The evolution naturally breaks down in time steps each ruled by a specific hierarchy of processes.

Electron excitation step. The electron gas is heated up by the pump pulse on a time scale of a few hundreds of femtoseconds, the maximum average electrons temperature $\max\{\langle T_e \rangle\}$ being attained within the 120 fs pulse duration. The value $\max\{\langle T_e \rangle\}$ is limited by the temperature-dependent electronic specific heat per unit volume and, to a lesser extent, by the electron-phonon interaction.

Electron-phonon thermalization step. The electron gas then cools raising $\langle T_{\rm ph} \rangle$. This process continues up to a time delay of few ps when $\langle T_e \rangle$ and $\langle T_{\rm ph} \rangle$ reach the common value of 301.8 K, the dynamic being better appreciated zooming the temperature scale, as reported in the bottom panel of Fig. 7. Starting from this instant one has $\langle T_{\rm ph} \rangle = \langle T_e \rangle$ and most of the Al film energy content is stored in the phonon gas, being $C_{\rm ph}/C_{el} \approx 10^2$. The difference between the phonon and electron specific heats also accounts for the fact that $\max\{\langle T_e \rangle\} \gg \max\{\langle T_{\rm ph} \rangle\}$. At this stage the temperature increase at the substrate interface is always rather small, amounting to ≈20% of its maximum excursion of 1 K, implying that, on these time scales, the Al film remains substantially isolated.

Film-substrate thermalization step. On longer time scales the Al film thermalizes with the substrate: $\langle T_{\rm ph} \rangle$ and $\langle T_e \rangle$ decrease together while T_{ic} attains its maximum value ≈100 ps after laser excitation and then decreases monotonously. T_{ic} now decreases because the energy flux from the metal overlay to the substrate interface is less than the energy flux from the latter to the Al_2O_3 bulk. This process ends after 1 ns when the Al film and substrate temperatures converge to the common value of 298.5 K.

Proximal-bulk substrate thermalization step. Starting from this instant the temperature drop across the interface is negligible as compared to the previous steps, $\Delta T \approx 0$. The metal overlay and the substrate portion proximal to the interface thermalize together with the Al_2O_3 bulk, the thermal dynamics being ruled solely by the sapphire thermal parameters through Eq. (9).

We now focus on the film-substrate thermalization step. It is in this step that a finite value of $R_{\rm ph}$ appreciably affects the film thermal dynamics as compared to the case of an isolated thin film where $R_{\rm ph} \to \infty$. For this same reason the TBR is retrieved from TR-TR experiments by detecting the thermally driven transient optical changes taking place during this step. The bottom panel of Fig. 7 shows that $T_{\rm ph}$ varies across the film thickness, its values being bound by the red dotted curves. The low temperature bound coincides with T_{ih} and occurs at

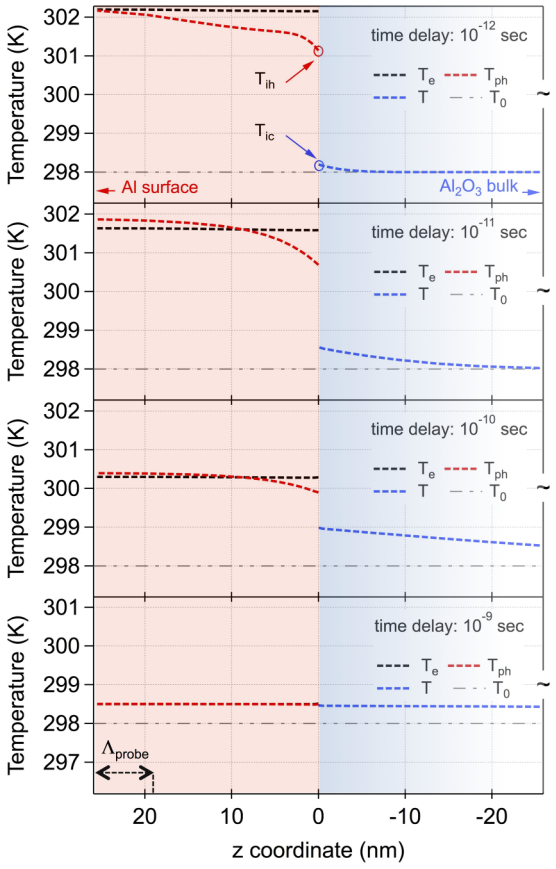

FIG. 8. Carrier temperatures across a portion of the sample thickness (z ∈ [−26 nm,26 nm]) at given time delays (in ascending order from 1 ps, top panel, to 1 ns, bottom panel) falling within the film-substrate thermalization step. The coordinate system and the colors assigned to the two materials follow the criteria adopted in the inset of the top panel of Fig. 7. Temperature profiles: metal electrons (black dashed line), metal phonons (red dashed line), substrate lattice (blue dashed line), and initial temperature (gray dash-dotted line). At greater depths, not reported in the present figure, the substrate temperature attains $T_0 = 298$ K. The laser probe penetration depth $\Lambda_{\rm probe} \approx 7$ nm is schematically reported in the bottom panel.

$z = 0+$, i.e., at the metal side of the interface, whereas the high temperature bound is found at the Al film surface, $z = 26$ nm. On the contrary T_e is spatially homogeneous across the film thickness. The bottom panel of Fig. 7 shows that the range of T_e values, bound by the black dotted lines, has negligible spread and $T_e = \langle T_e \rangle$ across the entire film thickness. These evidences also show that electron and phonon thermalization is far from being complete and continues throughout the entire step. The thermalization therein addressed refers to the fact that the electrons and phonons temperatures spatial averages have the same value.

Further physical insight is provided by inspection of the spatial temperatures distribution across the sample depth calculated at specific delay times limiting or falling within the film-substrate thermalization step; see Fig. 8. One ps after the pump pulse arrival $T_e \approx T_{\rm ph}$ within the first 6 nm from the film surface whereas deeper into the Al film $T_e \geqslant T_{\rm ph}$. The substrate temperature $T(z)$ remains substantially unaltered. The phonon

temperature drop across the interface is $\Delta T = 2.94$ K. For a time delay of 10 ps one finds $T_{\rm ph} \gtrsim T_e$ within the first 16 nm from the Al surface. This small temperature overshoot is due to the fact that electrons are losing energy not only to the phonon gas but also via diffusion to electrons located deeper into the film. Furthermore, the minute value of $\kappa_{\rm ph}$, as compared to κ_e, does not allow phonons in proximity of the surface to lose energy efficiently via diffusion to other film phonons. The interplay of these two effects leads to the above mentioned overshoot. Deeper into the substrate $T_{\rm ph}$ decreases rapidly and falls below T_e by as much as $\approx$0.9 K at the interface. Phonons in proximity of the interface, as opposed to phonons residing close to the surface, have an efficient energy loss pathway towards the phonons of the substrate thus preventing the phonon-electron temperature overshoot. The energy flux across the interface $J(t,z=0)$, from now on addressed as $J_{bd}(t)$, effectively raises T_{ic} above the T_0 baseline whereas the substrate bulk is not yet affected being $T(z \leqslant -20\ \text{nm}) = T_0$. Across the interface one finds $\Delta T = 2.12$ K. After 100 ps the electron and phonon temperatures spread across the Al depth diminishes. $J_{bd}(t)$ continued transferring energy to the substrate, resulting in a $\Delta T = 0.91$ K. Diffusion now plays a considerable role also in the substrate as may be appreciated inspecting $T(z)$ up to a depth of 26 nm from the interface. Furthermore, at this instant T_{ic} attains its maximum value and for longer time delays it will decrease; see blue curve in bottom panel of Fig. 7. This is due to heat diffusion becoming more efficient in dissipating energy from the cold side of the interface as compared to $J_{bd}(t)$ pumping energy into it. The snapshot taken 1 ns after laser excitation shows the film and the proximal portion of the substrate at roughly the same temperature and jointly thermalizing with the substrate bulk. The thermal dynamics for longer delay times is ruled by the Al_2O_3 lattice thermal conductivity κ via Eq. (9). One may thus expect a power-law scaling for the temperature profiles for long time delays.

The time-dependent spatial detachment between T_e and $T_{\rm ph}$ is ruled by the interplay of thermal parameters and film thickness. The temperature detachment diminishes upon increasing G and/or $R_{\rm ph}$, the latter consideration being of the utmost importance in view of extracting $R_{\rm ph}$ from experimental time-resolved traces.

B. Detection process: TBR from time resolved thermoreflectance

Knowledge of the carriers temperature evolution, as acquired via FEM modeling of the *excitation* process, allows one to link the optical reflectivity changes $\Delta\Re(t)$, taking place in TR-TR experiment, to the carrier thermal dynamics, and, ultimately, to the TBR. In the present work a laser probe wavelength of 780 nm is assumed.

Again, the focus is on the film-substrate thermalization step occurring on time scales exceeding few ps. The reflectivity variation reads [61,62]

$$\Delta\Re(t) = a\Delta T_e\big(t, z > L_{\rm Al} - \Lambda_{\rm probe}\big) + b\Delta T_{\rm ph}\big(t, z > L_{\rm Al} - \Lambda_{\rm probe}\big), \quad (10)$$

where $a = \partial\Re/\partial T_e$, $b = \partial\Re/\partial T_{\rm ph}$, $\Delta T_e(t,z) = T_e(t,z) - T_0$, $\Delta T_{\rm ph}(t,z) = T_{\rm ph}(t,z) - T_0$, $\Lambda_{\rm probe}$ is the laser probe penetration depth, and $z > L_{\rm Al} - \Lambda_{\rm probe}$ identifies the Al depth explored by the probe laser. Equation (10) holds since both $T_e(t,z)$ and $T_{\rm ph}(t,z)$ are substantially constants within a depth $\Lambda_{\rm probe} \approx 7$ nm from the Al surface for any time delay t. The spatial constancy strictly holds for $T_e(t,z)$ whereas a minimal z dependence sets in for $T_{\rm ph}(t, z > L_{\rm Al} - \Lambda_{\rm probe})$ on the sub-10 picoseconds time scale; see Fig. 8.

Equation (10) simplifies to $\Delta\Re(t) \propto \Delta T_e(t,z) = \Delta T_e(t)$. This is achieved upon inspection of Fig. 8 showing that (a) $\Delta T_{\rm ph}(t, z > L_{\rm Al} - \Lambda_{\rm probe}) \approx \Delta T_e(t, z > L_{\rm Al} - \Lambda_{\rm probe})$, the deviation being limited to the 10 ps time scale (b) $\Delta T_e(t,z)$ is actually spatially constant throughout the entire Al thickness and may thus be substituted for $\Delta T_e(t, z > L_{\rm Al} - \Lambda_{\rm probe})$ just writing $\Delta T_e(t)$. We remark that $\Delta T_e(t)$ is a functional of $R_{\rm ph}$, $\Delta T_e(t; R_{\rm ph})$.

In order to correctly retrieve $R_{\rm ph}$ from a TR-TR experiment one should therefore fit the experimental trace $\Delta\Re(t)$ with $\Delta T_e(t; R_{\rm ph})$ as obtained from FEM modeling (see Sec. IV A 1), taking $R_{\rm ph}$ as the fitting parameter. The value obtained from this fitting procedure should be taken as the benchmark against which theoretically calculated values are compared.

In the case of Al on sapphire experimental values for $R_{\rm ph}$ vary between $\approx$3.2 m^{2}K/GW [63] and $\approx$5.2 m^{2}K/GW [11,43], thus exceeding the value calculated in the present work [64]. We argue that the mismatch may be due to the fitting procedure adopted [11] to extract the TBR. In the TBR retrieval process the common ansatz is that, on time scales beyond tens of ps, the electrons and phonons within the metallic thin film (a) attain mutual thermal equilibrium, $T_e(t,z) = T_{\rm ph}(t,z)\ \forall z$, thus allowing one to define a unique thermodynamical temperature $T_{\rm Al}(t,z)$, and (b) the Biot number $\text{Bi} = (L_{\rm Al}/\kappa_{\rm Al})R_{\rm ph}^{-1} \ll 1$, where $\kappa_{\rm Al} = \kappa_{\rm ph} + \kappa_e$, thus allowing the metal film to be treated as a lumped thermal capacitance at temperature $T_{\rm Al}(t)$ (no z dependence) exchanging heat with the Al_2O_3 substrate at a temperature $T(t,z)$. In the seminal work of Ref. [11] the fit to the data is performed allowing for two fitting parameters, $R_{\rm ph}$ and κ. The best fit is obtained with $R_{\rm ph} = 5.2$ m^{2}K/GW and a value of κ overestimating by a factor of 4 the value reported in the literature for bulk Al_2O_3. This suggests that the ansatz behind the fitting model may not be valid, a fact that clearly emerges in our simulations where the electron and phonon temperatures at the interface remain decoupled over several time decades and the phonon temperature is spatially inhomogeneous, see Fig. 8. In order to further substantiate this point we fitted $\Delta\Re(t)$ as retrieved from our theoretical calculations, $\Delta\Re(t) \propto \Delta T_e(t)$, with the lumped thermal capacitance model. We allowed $R_{\rm ph}$ as the only fitting parameter. The fit was performed on the trace ΔT_e, as obtained from Fig. 7 upon subtraction of the baseline temperature of 298 K. The best fit overestimates by a factor of $\approx$2 the theoretical value of $R_{\rm ph} = 1.44$ m^{2}K/GW used to calculate ΔT_e. Assuming experimental values were overestimated by the same factor leads to a convergence between experimental results and the results obtained from NEMD in Sec. III C.

Let us now address the physical explanation of why a fit based on the lumped thermal capacitance model overestimates the actual TBR. The TBR is defined by means of the phonons temperatures on both sides of the interface,

$R_{\rm ph} = (T_{ih} - T_{ic})/J_{bd}$, whereas the probe is sensitive to the temperature dynamics taking place within a depth $\Lambda_{\rm probe}$ from the free Al surface, $\Delta T_e = T_e(t, z > L_{\rm Al} - \Lambda_{\rm probe}) - T_0$. Our calculations show that the temperature entering the definition of TBR, i.e., the phonon temperature on the metal side of the interface, deviates from the temperature of the probed region. On the other hand, a lumped thermal capacitance model implies a unique temperature common to both electrons and phonons throughout the entire Al film thickness leading to an overestimation of T_{ih} in the expression for $R_{\rm ph}$, and, ultimately, of the $R_{\rm ph}$ value itself. All in all, within the lumped thermal capacitance model, the red dashed curve for $T_{\rm ph}$ shown in Fig. 8 is made to coincide with the black dashed curve for T_e throughout the entire Al depth. On a general basis the lumped thermal capacitance model may be retrieved from our model for $R_{\rm ph} \to \infty$. Indeed, should an interface bear a high enough TBR, the phonon temperature would be spatially homogeneous and match the electronic temperature throughout the entire metal film depth. Nevertheless, from an experimentalist point of view, the TBR is not known *a priori*; hence the full thermodynamical approach, accounting for electron and phonon temperatures spatiotemporal decoupling via the TTM, should be exploited to fit the experimental TR-TR traces in order to retrieve the TBR.

C. Steady-state vs transient nanocalorimetry

The results presented in the two previous subsections apply to *transient* nanocalorimetry across a metal-insulating interface. Our results account for the effects of both phonons and electrons (with the exclusion of the *direct* coupling mechanism between the metal's electrons and the substrate's phonons addressed at the end of Sec. III C) and provide a protocol to access TBR from TR-TR measurements. At the light of our findings we now review literature's results in the frame of *steady-state* heat transport.

In recent years extensive effort has been devoted to account for the effects of both electrons and phonons in the frame of *steady-state* heat transport across a metal-insulator heterojunction. Steady-state heat transport may be achieved for instance by placing a hot (cold) temperature reservoir in contact with the metal (insulator) end. The question then arises as to which *overall* thermal resistance $R_{\rm tot}$ one actually accesses when performing a steady-state measurement with the scope of retrieving the TBR, given the presence of conducting electrons exchanging energy with phonons on the metal side of the interface. $R_{\rm tot}$ encloses the contributions from all thermal resistances comprised between the two thermal leads, that is the thermal resistances within the metal's and insulator's bulk and $R_{\rm ph}$. It has been argued [10,65,66] that, due to electron-phonon coupling, electrons may have a strong impact on $R_{\rm tot}$. Majumdar and Reddy [10] found the analytical expression incorporating such contribution in the case of a infinitely thick metal layer in contact with an insulating substrate, suggesting that, due to electron-phonon coupling, electrons contribute a series resistance, R_{ep}, to the overall $R_{\rm tot}$. Ordonez-Miranda *et al.* [67] improved the model including the effect of the finiteness of the metal layer, an essential step forward in view of modeling actual experiments. The model describes the electrons and phonons in the metal with a steady-state version of the TTM. The time-dependent terms on the left side of Eqs. (5) and (6) are set to zero and the impulsive heating term P_p is missing. Continuity of the heat flux across the interface involves phonons only and is achieved via Eqs. (7) and (8). The phonon thermal dynamics on the insulator side of the interface is accounted for by Laplace's equation. Dirichlet (first-type) boundary conditions are enforced on the external boundaries of the system, where the metal's electrons and phonons are kept at a temperature $T_{\rm hot}$ and the substrate's phonons at $T_{\rm cold}$. This is at variance with the insulating boundary conditions necessary to describe the impulsively heated metal film. The model has a straightforward analytic solution as opposed to our case. The electrons, $T_{ih,e}$, and phonons, T_{ih}, temperatures at the metal side of the interface are found to be different. Defining $R_{\rm tot} = (T_{\rm hot} - T_{\rm cold})/J$, where J is the steady-state heat flux across the sample, one obtains

$$R_{\rm tot} = \frac{L_{\rm Al}}{\kappa_e + \kappa_{\rm ph}} + R_{\rm ph} + \frac{L_{\rm Al_2O_3}}{\kappa} + R_{ep}, \qquad (11)$$

where the thermal resistance R_{ep} arises because of the presence of the electron-phonon coupling and has a simple analytical expression [68]. R_{ep} is often addressed as the electronic contribution to the TBR. This is due to the fact that the electron and phonon temperatures decoupling is strongest at the interface, a common feature regardless of the *transient* or *static* nature of the problem. For the sake of clarity we stress that R_{ep} has nothing to do with R_e ruling the *direct* coupling mechanism between the metal electrons and the substrate phonons addressed at the end of Sec. III C. The TBR is thus obtained measuring $R_{\rm tot}$ in steady-state experiments and extracting $R_{\rm ph}$ from Eq. (11).

This model might correctly predict $R_{\rm tot}$ in steady-state experiments provided that the electron and phonon temperatures at the hot metal end can actually be set to the same value in a true experiment. This is not obvious since, in the real case, an interface (junction) might be present between the circuit connecting lead and the Al slab. However, the model cannot be used to describe the thermal dynamics occurring in TR-TR. As a matter of fact in time-resolved nanocalorimetry a finite energy is impulsively delivered to the metal as opposed to fixing the temperature at the metal extremity. One is thus faced with a *transient* as opposed to a steady-state thermal problem. Despite this fact the steady-state formulation has been adopted to discuss the TBR retrieved from TR-TR experiments [10,65]. This is possibly due to its elegant analytical solution, explicating in a simple formula the relevant thermal and geometrical parameters involved.

V. CONCLUSIONS

In the present work the thermal boundary resistance in the paradigmatic nanometric Al film-sapphire heterojunction has been investigated by means of nonequilibrium molecular dynamics. A strategy has been devised to considerably reduce the computational burden, allowing one to simulate a system of realistic size. The approach is readily transferable to other heterojunctions. The TBR was found to be monotonously decreasing with interface temperature in the range 300–400 K, the room temperature value being $\approx$1.4 m^{2}K/GW. The effect of the calculated TBR on the thermal dynamics occurring

in an all-optical time-resolved nanocalorimetry experiment was theoretically addressed casting the problem in terms of continuous macrophysics equations and solving them by finite element methods. The electrons and phonons within the Al films were found to remain out of mutual equilibrium up to 1 ns delay times. Whereas the electronic temperature is spatially constant throughout the metal film depth, the same does not hold for the phonon temperature, its spatial gradient attaining the maximum value in proximity of the metal-insulator interface. Knowledge of the spatiotemporal carrier dynamics allowed us to link the optical reflectivity changes to the TBR, thus providing a protocol to extract the latter from real experiments. The procedure adopted in the literature to extract TBR from experimental results was revised in the light of the present findings, improving the congruency between theoretical predictions and experimental findings. A comparison with models addressing TBR in the frame of steady-state heat transfer experiment was finally presented.

The present understanding goes beyond the specific system here investigated and it may be applied to other metal-insulator heterojunctions.

ACKNOWLEDGMENTS

C.C. and F.B. acknowledge financial support from the MIUR Futuro in ricerca 2013 Grant in the frame of the ULTRANANO Project (Project No. RBFR13NEA4). F.B., G.F., and C.G. acknowledge support from Università Cattolica del Sacro Cuore through D.2.2 and D.3.1 grants. F.B. and G.F. acknowledge financial support from Fondazione E.U.L.O. R.R. acknowledges financial support by the Ministerio de Economía, Industria y Competitividad (MINECO) under Grant No. FEDER-MAT2013-40581-P and the Severo Ochoa Centres of Excellence Program under Grant No. SEV-2015-0496 and by the Generalitat de Catalunya under Grant No. 2014 SGR 301. We thank Marco Gandolfi and Daniele Scopece for enlightening discussions.

APPENDIX A: COMPUTATIONAL DETAILS

All simulations have been performed with the LAMMPS package [69]. Among others [70,71] we selected the Streitz-Mintmire potential for Al and Al_2O_3, where the total energy is given by the sum of the electrostatic energy and a standard embedded atom method potential (EAM) [72,73]. The potential allows a dynamical self-consistent calculation of the atomic partial charges to take into account the charge transfer between the oxide and the metal at the interface. Electrostatic interactions have been calculated with the Wolf summation method [74], with cutoff $\rho = 8$ Å and damping parameter $\alpha = 0.11$ Å^{-1}. The adopted potential has been tested against several properties of Al and Al_2O_3 (e.g., lattice constants, cohesive energies, and elastic constants), providing a very good agreement with experimental and *ab initio* data [72,73]. The temperature was controlled by a Nosé-Hoover thermostat while the equations of motion have been integrated by a time step as short as 1 fs.

APPENDIX B: ABSORBED POWER DENSITY

The space-time profile for the pulsed power per unit volume absorbed by the sample is $P_p(r,t) = P_{\mathbf{r}}(z,r)P_t(t)$. The time profile reads $P_t(t) = (1/\sqrt{2\pi})\exp[(t-t_0)^2/2\tau_p^2]$ with $\tau_p = 120$ fs the pulse time duration at FWHM. The spatial profile is factorable as $P_{\mathbf{r}}(r,z) = P_r(r)P_z(z)$. The radial intensity distribution $P_r(r)$ is Gaussian with a FWHM $= 55$ μm. The monotonously decreasing in-depth profile $P_z(z)$ is obtained solving for the electromagnetic field distribution in the the Al film-Al_2O_3 substrate for a laser wavelength of 780 nm via the standard transfer matrix method and, based on this, calculating the power absorbed per unit volume in the film [75]. The analytic z spatial dependence is therefore not explicit. Nevertheless, since the pump laser penetration depth $\Lambda_{\text{pump}} = 7$ nm is smaller than the Al film's thickness of 26 nm, $P_z(z)$ is similar to the standard in-depth exponential absorption profile, obtained assuming a semi-infinite Al slab (see, for instance, Ref. [76]). As a matter of fact the standard in-depth exponential absorption profile could have been employed without substantially affecting the present results. As for the laser pump beam-sample interaction the optical constants of Al and sapphire at 780 nm wavelength have been taken from the literature; see Table I in Appendix C. In a nutshell, the optical constants of Al in the 800 nm range are well mimicked by a Lorentz-Drude model where, besides the Drude term, a Lorentz oscillator centered at an energy of 1.56 eV has been introduced so as to account for a critical point in the Al joint density of states; refer to Ref. [56] for further details.

APPENDIX C: TABLE OF MATERIALS PARAMETERS

For the sake of readability in the following table we summarize the materials parameters values adopted for FEM simulations.

TABLE I. Summary of materials parameters values adopted for FEM simulations. Legend: [*] values obtained in the present work (Sec. III); [a] $\kappa_e = \kappa_{\text{Al}} - \kappa_{\text{ph}}$ with $\kappa_{\text{Al}} = 237$ W m^{-1}K^{-1} from Ref. [77] and κ_{ph} obtained from NEMD calculations (Sec. III).

Parameter	Value	Units	Ref.
γ_e	95	J m^{-3}K^{-2}	[51]
C_{el}	$\gamma_e T_e$	J m^{-3}K^{-1}	[51]
C_{ph}	2.48×10^6	J m^{-3}K^{-1}	[50,52]
C	3.09×10^6	J m^{-3}K^{-1}	[59]
κ_e	230	W m^{-1}K^{-1}	[a]
κ_{ph}	7.12	W m^{-1}K^{-1}	[*]
κ	32.5	W m^{-1}K^{-1}	[*]
G	2.45×10^{17}	W m^{-3}K^{-1}	[53]
R_{ph}	1.44×10^{-9}	W^{-1}m^{2}K	[*]
Re($\tilde{n}_{\text{Al}}$)	2.58		[56]
Im($\tilde{n}_{\text{Al}}$)	8.4		[56]
Re($\tilde{n}_{\text{Al}_2\text{O}_3}$)	1.76		[57]

[1] G. Chen, *Nanoscale Energy Transport and Conversion* (Oxford University Press, Oxford, 2005).

[2] T. Luo and G. Chen, Phys. Chem. Chem. Phys. **15**, 3389 (2013).

[3] D. G. Cahill, P. V. Braun, G. Chen, D. R. Clarke, S. Fan, K. E. Goodson, P. Keblinski, W. P. King, G. D. Mahan, A. Majumdar *et al.*, Appl. Phys. Rev. **1**, 011305 (2014).

[4] K. M. Hoogeboom-Pot, J. N. Hernandez-Charpak, X. Gu, T. D. Frazer, E. H. Anderson, W. Chao, R. W. Falcone, R. Yang, M. M. Murnane, H. C. Kapteyn *et al.*, Proc. Natl. Acad. Sci. U.S.A. **112**, 4846 (2015).

[5] E. T. Swartz and R. O. Pohl, Rev. Mod. Phys. **61**, 605 (1989).

[6] A. L. Moore and L. Shi, Mater. Today **17**, 163 (2014).

[7] E. Pop, Nano Res. **3**, 147 (2010).

[8] E. S. Landry and A. J. H. McGaughey, Phys. Rev. B **80**, 165304 (2009).

[9] R. M. Costescu, M. A. Wall, and D. G. Cahill, Phys. Rev. B **67**, 054302 (2003).

[10] A. Majumdar and P. Reddy, Appl. Phys. Lett. **84**, 4768 (2004).

[11] R. J. Stoner and H. J. Maris, Phys. Rev. B **48**, 16373 (1993).

[12] D. G. Cahill, W. K. Ford, K. E. Goodson, G. D. Mahan, A. Majumdar, H. J. Maris, R. Merlin, and S. R. Phillpot, J. Appl. Phys. **93**, 793 (2003).

[13] M. E. Siemens, Q. Li, R. Yang, K. A. Nelson, E. H. Anderson, M. M. Murnane, and H. C. Kapteyn, Nat. Mater. **9**, 26 (2010).

[14] V. Juvé, M. Scardamaglia, P. Maioli, A. Crut, S. Merabia, L. Joly, N. Del Fatti, and F. Vallée, Phys. Rev. B **80**, 195406 (2009).

[15] F. Banfi, V. Juvé, D. Nardi, S. D. Conte, C. Giannetti, G. Ferrini, N. D. Fatti, and F. Vallée, Appl. Phys. Lett. **100**, 011902 (2012).

[16] T. Stoll, P. Maioli, A. Crut, S. Rodal-Cedeira, I. Pastoriza-Santos, F. Vallée, and N. Del Fatti, J. Phys. Chem. C **119**, 12757 (2015).

[17] M. N. Ozisik, *Heat Conduction* (John Wiley & Sons, New York, 1993).

[18] J. Lombard, F. Detcheverry, and S. Merabia, J. Phys.: Condens. Matter **27**, 015007 (2014).

[19] N. Chkhalo, M. Fedorchenko, A. Zarodyshev, V. Chernov, V. Kirillov, and A. Nikiforov, Nucl. Instrum. Methods, Phys. Res. A **359**, 127 (1995).

[20] D. Nardi, E. Zagato, G. Ferrini, C. Giannetti, and F. Banfi, Appl. Phys. Lett. **100**, 253106 (2012).

[21] M. Ksiazek, N. Sobczak, B. Mikulowski, W. Radziwill, and I. Surowiak, Mater. Sci. Eng. A **324**, 162 (2002).

[22] Refer to Ref. [78] for a review of NEMD and a thorough discussion on different formalisms available for calculating TBR.

[23] C. Melis, G. Barbarino, and L. Colombo, Phys. Rev. B **92**, 245408 (2015).

[24] D. P. Sellan, E. S. Landry, J. E. Turney, A. J. H. McGaughey, and C. H. Amon, Phys. Rev. B **81**, 214305 (2010).

[25] C. Melis, R. Dettori, S. Vandermeulen, and L. Colombo, Eur. Phys. J. B **87**, 96 (2014).

[26] G. Balasubramanian and I. K. Puri, Appl. Phys. Lett. **99**, 013116 (2011).

[27] M. Vermeersch, R. Sporken, P. Lambin, and R. Caudano, Surf. Sci. **235**, 5 (1990).

[28] M. Vermeersch, F. Malengreau, R. Sporken, and R. Caudano, Surf. Sci. **323**, 175 (1995).

[29] D. Medlin, K. McCarty, R. Hwang, S. Guthrie, and M. Baskes, Thin Solid Films **299**, 110 (1997).

[30] D. J. Siegel, L. G. Hector, and J. B. Adams, Phys. Rev. B **65**, 085415 (2002).

[31] G. Pilania, B. J. Thijsse, R. G. Hoagland, I. Lazić, S. M. Valone, and X.-Y. Liu, Sci. Rep. **4**, 4485 (2014).

[32] H. Mei, Q. Liu, L. Liu, X. Lai, W. She, and P. Zhai, Appl. Surf. Sci. **324**, 538 (2015).

[33] D. G. Cahill, S.-M. Lee, and T. I. Selinder, J. Appl. Phys. **83**, 5783 (1998).

[34] O. N. Bedoya-Martínez, J.-L. Barrat, and D. Rodney, Phys. Rev. B **89**, 014303 (2014).

[35] D. Singh, J. Y. Murthy, and T. S. Fisher, J. Appl. Phys. **110**, 044317 (2011).

[36] A. Jain and A. J. H. McGaughey, Phys. Rev. B **93**, 081206 (2016).

[37] Y. Wang, Z. Lu, and X. Ruan, J. Appl. Phys. **119**, 225109 (2016).

[38] Z. Liang and P. Keblinski, Phys. Rev. B **90**, 075411 (2014).

[39] J. Chen, G. Zhang, and B. Li, J. Appl. Phys. **112**, 064319 (2012).

[40] D. Nardi, M. Travagliati, M. E. Siemens, Q. Li, M. M. Murnane, H. C. Kapteyn, G. Ferrini, F. Parmigiani, and F. Banfi, Nano Lett. **11**, 4126 (2011).

[41] F. Banfi, F. Pressacco, B. Revaz, C. Giannetti, D. Nardi, G. Ferrini, and F. Parmigiani, Phys. Rev. B **81**, 155426 (2010).

[42] C. Giannetti, F. Banfi, D. Nardi, G. Ferrini, and F. Parmigiani, Photon. J. IEEE **1**, 21 (2009).

[43] P. E. Hopkins, R. N. Salaway, R. J. Stevens, and P. M. Norris, Int. J. Thermophys. **28**, 947 (2007).

[44] R. Rurali, L. Colombo, X. Cartoixà, Ø. Wilhelmsen, T. T. Trinh, D. Bedeaux, and S. Kjelstrup, Phys. Chem. Chem. Phys. **18**, 13741 (2016).

[45] H.-K. Lyeo and D. G. Cahill, Phys. Rev. B **73**, 144301 (2006).

[46] P. E. Hopkins and P. M. Norris, ASME J. Heat Transfer **131(2)**, 022402 (2009).

[47] S. Sadasivam, U. V. Waghmare, and T. S. Fisher, J. App. Phys. **117**, 134502 (2015).

[48] A. V. Sergeev, Phys. Rev. B **58**, R10199 (1998).

[49] M. I. Kaganov, I. M. Lifshitz, and L. V. Tanatarov, Zh. Eksp. Teor. Fiz. **31**, 232 (1957) [Sov. Phys. JETP **4**, 173 (1957)].

[50] F. Cverna, *ASM Ready Reference: Thermal Properties of Metal* (ASM International, Materials Park, OH, 2002).

[51] P. B. Allen, Phys. Rev. B **36**, 2920 (1987).

[52] Z. Lin, L. V. Zhigilei, and V. Celli, Phys. Rev. B **77**, 075133 (2008).

[53] J. L. Hostetler, A. N. Smith, D. M. Czajkowsky, and P. M. Norris, Appl. Opt. **38**, 3614 (1999).

[54] The value $\kappa_{\mathrm{Al}} = \kappa_e + \kappa_{\mathrm{ph}}$ with $\kappa_{\mathrm{Al}} = 237$ W m^{-1}K^{-1} from Ref. [77], whereas $\kappa_{\mathrm{ph}} = 7$ W m^{-1}K^{-1} is obtained from NEMD calculations in Sec. III; hence $\kappa_e = 230$ W m^{-1}K^{-1}.

[55] The actual numerics has been implemented assigning the proper symmetry to P_p, $P_p = P_p(r,z,t)$, as dictated by the pump laser Gaussian profile; nevertheless, within the probed area, the problem is substantially 1D.

[56] A. D. Rakić, A. B. Djurišić, J. M. Elazar, and M. L. Majewski, Appl. Opt. **37**, 5271 (1998).

[57] I. H. Malitson, J. Opt. Soc. Am. **52**, 1377 (1962).

[58] As discussed in Sec. III C, the value R_{ph} does not depend on the Al thickness, the small fluctuations reported in Fig. 5 being due to numerical instabilities.

[59] M. J. Weber, *Handbook of Optical Materials* (CRC Press, Boca Raton, FL, 2001).

[60] As for the initial conditions we have checked the effect of the cumulative effect of the train of pulses from a cavity-dumped

laser apparatus with repetition rate of 1 MHz (a cavity damped system has been assumed in order to avoid excessive cumulated heating) following Ref. [42]. The outcome is that, given the present laser parameters and materials combination, assuming a spatially constant temperature $T_0 = 298$ K is a reasonable approximation.

[61] P. M. Norris, A. P. Caffrey, R. J. Stevens, J. M. Klopf, J. T. McLeskey, Jr., and A. N. Smith, Rev. Sci. Instrum. **74**, 400 (2003).

[62] C. Giannetti, M. Capone, D. Fausti, M. Fabrizio, F. Parmigiani, and D. Mihailovic, Adv. Phys. **65**, 58 (2016).

[63] P. E. Hopkins, K. Hattar, T. Beechem, J. F. Ihlefeld, D. L. Medlin, and E. S. Piekos, Appl. Phys. Lett. **98**, 231901 (2011).

[64] Reference [11] reports in the main text a value of $R_{\mathrm{ph}} \approx 10$ m^{2}K/GW; nevertheless, upon digitizing the experimental values therein reported, we retrieve 5.5 m^{2}K/GW.

[65] Y. Wang, X. Ruan, and A. K. Roy, Phys. Rev. B **85**, 205311 (2012).

[66] D. Campi, D. Donadio, G. C. Sosso, J. Behler, and M. Bernasconi, J. Appl. Phys. **117**, 015304 (2015).

[67] J. Ordonez-Miranda, J. J. Alvarado-Gil, and R. Yang, J. Appl. Phys. **109**, 094310 (2011).

[68] The explicit expression for R_e is the fourth term on the right side of Eq. (11) in Ref. [42].

[69] S. Plimpton, J. Comput. Phys. **117**, 1 (1995).

[70] I. Lazić and B. J. Thijsse, Comput. Mater. Sci. **53**, 483 (2012).

[71] D. Scopece and B. J. Thijsse, Comput. Mater. Sci. **104**, 143 (2015).

[72] F. H. Streitz and J. W. Mintmire, Phys. Rev. B **50**, 11996 (1994).

[73] X. W. Zhou, H. N. G. Wadley, J.-S. Filhol, and M. N. Neurock, Phys. Rev. B **69**, 035402 (2004).

[74] D. Wolf, P. Keblinski, S. R. Phillpot, and J. Eggebrecht, J. Chem. Phys. **110**, 8254 (1999).

[75] F. Abeles, *Optics of Thin Films* (North-Holland, Amsterdam, 1967).

[76] C. Giannetti, B. Revaz, F. Banfi, M. Montagnese, G. Ferrini, C. F, S. Maccalli, P. Vavassori, G. Oliviero, E. Bontempi *et al.*, Phys. Rev. B **76**, 125413 (2007).

[77] N. Ashcroft and N. D. Mermin, *Solid State Physics* (Saunders College Publishers, Philadelphia, 1976).

[78] R. Dettori, C. Melis, X. Cartoixà, R. Rurali, and L. Colombo, Adv. Phys. X **1**, 246 (2016).